



Ice albedo and its relationship with light-absorbing impurities and weathering crust at the Potanin Glacier, Mongolia

Akiko Sakai¹, Kino Kobayashi², Masato Ono³, Sayako Ueda¹, Sho Ohata⁴, Akira Watanabe⁵, Kazuo
5 Osada¹, Nozomu Takeuchi⁶, Khalzan Prevdagva⁷, Sumito Matoba⁸, Tomonori Tanikawa⁹ and Teruo
Aoki⁹

¹ Graduate School of Environmental Studies, Nagoya University, Japan

² Graduate School of Science and Engineering, Chiba University, Japan

10 ³ Center for Ecological Research, Kyoto University, Japan

⁴ Institute for Space–Earth Environmental Research, Nagoya University, Japan

⁵ Graduate School of Bioagricultural Sciences, Nagoya University, Japan

⁶ Graduate School of Science, Chiba University, Japan

⁷ Information and Research Institute of Meteorology Hydrology and Environment, Mongolia

15 ⁸ Institute of Low Temperature Science, Hokkaido University, Japan

⁹ Meteorological Research Institute, Japan Meteorological Agency, Japan

Correspondence: Akiko Sakai (shakai@nagoya-u.jp)

20 **Abstract.** The glacier ablation areas in the mid-latitude mountains have a dark surface due to abundant
light-absorbing impurities (LAIs) (mineral dust, organic matter of microbial origin, black carbon).
Conversely, the development of weathering crust on the bare ice surface increases the surface albedo.
During the summers of 2022 to 2024, field observations were conducted on the Potanin Glacier in
Mongolia. In this study, we defined the low-density surface layer within the weathering crust as the
25 weathering granular ice layer. Here, we clarify the relationship between broad-band albedo (BB
albedo), the thickness of surface granular ice, and LAI content within the granular ice layer. In situ
measurements of the BB albedo showed a significant positive correlation with the thickness of the
granular ice layer, but a relatively strong negative correlation with organic matter. It was also revealed
30 that higher concentrations of LAIs inhibited the thickening of the weathering crust layer. Furthermore,
the observed variability in correlation strength across different impurity concentrations, together with
evidence from previous studies, suggests that mineral particles, whether exposed within the glacier or
deposited onto the glacier surface from the atmosphere, support the growth of microorganisms living
on the ice. The subsequent proliferation of these microorganisms and the production of humic-like
35 substances are considered to increase surface adhesiveness, thereby facilitating the adsorption of black
carbon.



1 Introduction

Mountain glaciers have been shrinking in recent years due to global warming (Hugonnet et al., 2021; 40 The GlaMBIE Team, 2025). Accurately projecting the mass balance of glaciers is therefore crucial. Net shortwave radiation is the primary heat source for glacier melting in most cases (e.g., Braithwaite, 1995; Greuell and Smeets, 2001; Pellicciotti et al., 2005). The albedo is crucial to this melting process because it determines the fraction of downward shortwave radiation reflected, which, in turn, affects the incoming shortwave radiation. Clean snow and ice have relatively high albedos. However, LAIs 45 such as mineral dust, black carbon, and microorganisms significantly reduce albedo, thereby substantially increasing the absorption of shortwave radiation. Recent studies in Europe have revealed a significant correlation between the minimum summer albedo values of individual glaciers and their annual mass balance (Di Mauro and Fugazza, 2022).

Important factors that determine the albedo of a snow surface are the size of the snow particles and 50 the concentration of light-absorbing impurities (LAIs)—substances such as mineral dust and black carbon that reduce how much light is reflected (e.g., Warren, 1982; Aoki et al., 2003; Flanner and Zender, 2006; Painter et al., 2001). Albedo reduction due to LAIs has been documented in previous studies (e.g., Warren and Wiscombe, 1980; Flanner et al., 2007; Dumont et al., 2017; Skiles and Painter, 2017). Physically based snow albedo models that account for radiative transfer processes 55 within the snow layer have been developed by several researchers: SNICAR (Flanner et al., 2021), PBSAM (Aoki et al., 2011), and TARTES (Picard et al., 2024). Recently, biological impurities (such as algae that grow on snow) that also affect albedo reduction have been studied (Cook et al., 2017a; Onuma et al., 2020; Halbach et al., 2022). Cook et al. (2017b) included biological impurities in radiative transfer models. They compared the albedo reductions caused by bioalbedo (albedo reduction 60 due to biological impurities) and BC (black carbon), showing that bioalbedo is more effective at reducing snow albedo.

However, albedo's effect on glacier melting is especially important in ablation areas, where the 'ice' surface is exposed. Surface albedo here strongly impacts glacier mass balance (Naegeli et al., 2017). Observations of albedo in ablation areas are limited. Hartl et al. (2020) summarised bare-ice albedo 65 observations on glaciers. They measured spectral reflectance (HCRF, spherical–conical reflectance factors) of bare ice. They classified ice as wet or dry, non-debris or debris, then compared these types with LANDSAT imagery. Whicker et al. (2022) developed a spectral albedo model for glacier ice, SNICAR-ADv4, which includes LAI. They recommended setting a thin layer of snow over bare ice. Furthermore, in the ablation zone where ice surfaces are exposed, penetration of solar radiation into 70 the ice induces subsurface melting, leading to the formation of a porous, mechanically fragile weathering crust. Weathering crust and LAI are important factors increasing albedo in glacier ablation areas (Tedstone et al., 2020). Weathering crust observations were conducted in Greenland (Cook et al.,



2016; Irvine-Fynn et al., 2021), Alaska (Christner et al., 2018) and East Antarctica (Traversa and Di
75 Mauro, 2024). Woods and Hewitt (2023) modelled weathering crust based on microbial activity and
chemical composition, assuming it exists in Greenland. They found that shortwave (surface-
penetrating) radiation is significant for weathering crust structure.

In High Mountain Asia, glaciers have heavier abundances of mineral dust, black carbon, and
microorganisms on their surfaces than glaciers in Patagonia, Alaska, and the Arctic regions (Takeuchi
80 et al., 2005; Takeuchi et al., 2008). These light-absorbing impurities are therefore expected to have a
strong impact on reducing ice albedo. In addition, the development of a weathering crust quantitatively
increases surface albedo. However, to date, only Takeuchi et al. (2005) have investigated weathering
crust on glaciers in High Mountain Asia. Granular ice has been observed by Zhang et al. (2017) and
Li et al. (2017). It has been reported that granular ice contains as many impurities (mineral dust and
85 black carbon) as old snow. These impurities contribute to albedo reduction. While the role of LAIs in
albedo reduction is well studied, there has been no research in High Mountain Asia explicitly
investigating how weathering crust and surface granular ice relate to impurities and affect albedo.

In this study, we focused not only on LAIs but also on weathering crust, especially the granular ice in
the surface layer. We performed investigations and analyses to clarify the relationships between albedo
and these elements. We targeted mineral dust (MD), black carbon (BC), and organic matter (OM) as
90 the three major LAIs. The aim of this study is to elucidate the interrelationships among light-absorbing
impurities (LAIs) and between surface granular ice and LAIs in the High Mountain Asia (HMA), and
to clarify the differing roles of each LAI in glacier surface albedo reduction and in influencing the
development of the weathering crust.

95

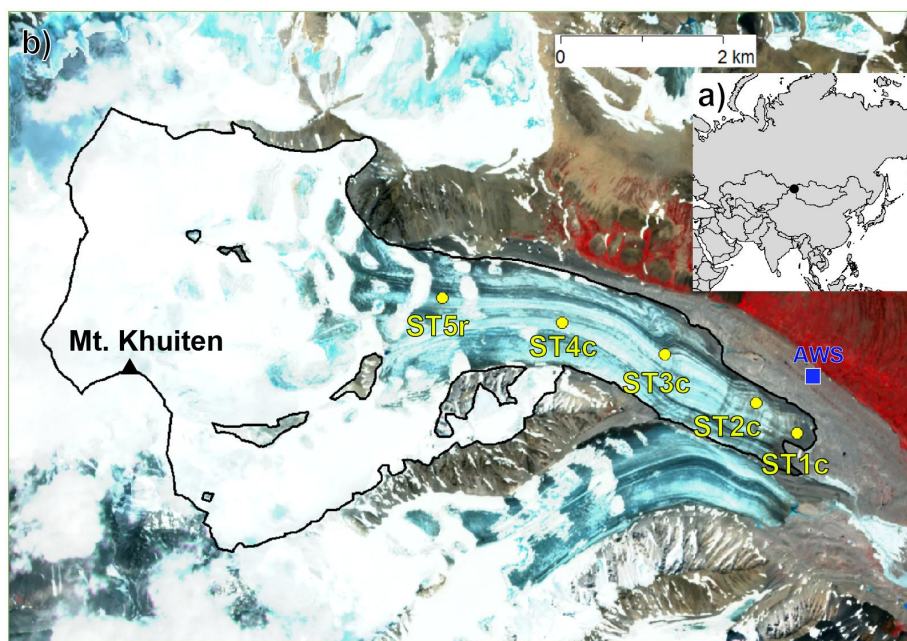
2 Observation

2.1 Study area and previous study

100 We conducted field observations at the Potanin Glacier (87.866°E, 49.154°N), which is located in the
northern part of the HMA, on the western edge of Mongolia (Fig. 1a). In this region, glaciers are
classified as summer accumulation type, and about 80% of annual precipitation falls in summer
(Khalzan et al., 2022). In Mongolia, research has been conducted on observations and modelling of
glacier mass balance (Khalzan et al., 2022) and runoff (Pan et al., 2019; Kalzhan et al., 2025), as well
105 as glacier area changes (Pan et al., 2017). Kalzhan et al. (2025) reported that glacier meltwater
accounted for 28% of river runoff even though the glacier area ratio was only 0.8% in the upper Ulgii
basin, including the Potanin Glacier, from 2000 to 2020. The large runoff from glaciers would be due
to recent glacier shrinkage.



110 The Potanin Glacier in the Tavan Bogd region reaches a maximum elevation of 4,374 m a.s.l. (Mt. Khuiten). Its terminus sits at 2,907 m a.s.l. The glacier is 10.4 km long and covers 24.7 km², making it the largest in Mongolia. Mass balance data have been collected since 2003 (Khalzan et al., 2022). The estimated glacier-wide mass balance at the Potanin Glacier is -158 ± 258 mm w.e. yr⁻¹ from 1980 to 2018, using optimised precipitation data (Khalzan et al., 2022).



115

Figure 1. Location map of the Potanin Glacier a) and observed stake location at the Potanin Glacier b). The edges of the Potanin glacier are outlined in black. The back satellite imagery is Sentinel 2 acquired on 15 July 2023.

120

2.2 Observation and sample analysis

125 Field observations were conducted during the ablation season in July-August 2022, 2023, and 2024. The sampling periods varied each year: July 3rd to 11th in 2022, July 4th to August 8th in 2023, and July 22nd to August 2nd in 2024.



2.2.1 Shallow ice cores for ice density profile at depth

130

We took two shallow ice cores at ST2c and ST3c (Fig. 1b) in July 2023 using an ice auger (Olympia Kogyo Co., LTD.) to obtain an ice density-depth profile, including the weathering crust. For each separated ice core, we measured the weight, length, and cross-sectional diameter at the drilling site using a calliper. We also measured the thickness of the weathering crust at the same sites.

135

2.2.2 LAIs, surface granular ice thickness and BB albedo

At the Potanin Glacier, the uppermost part of the weathering crust features a layer with particularly low ice density, characterised by a granular ice texture. The boundary between this layer and the underlying high-density crust layer can be easily identified and is referred to in this study as the surface granular ice layer. The thickness of the surface granular ice layer was used as an indicator of the degree of weathering crust development (see Section 3.1 for observation results). This layer contains exceptionally high concentrations of light-absorbing impurities (LAIs). It can be regarded as corresponding to the dirt surface layer (Ueda et al., preprint).

140

We performed the following measurements and sampling to investigate the relationships among broadband albedo (BB albedo), the three major LAIs (MD: Mineral dust, OM: Organic matter, BC: Black carbon), and granular ice thickness (GIT) of the weathering crust. BB albedo is defined as the surface albedo integrated over a certain wavelength range. Here, we define BB albedo as the fraction of the total incoming solar radiation reflected by a surface over the entire shortwave spectral range.

145

There are five stakes (ST1c, ST2c, ST3c, ST4c, ST5r) along the central line of the ablation area (Fig. 1b), from which we collected impurities on the glacier surface. At two to ten sites near each stake, we measured broadband (BB) albedo and collected impurity samples, avoiding snow surfaces. Debris from the nunatak accumulates and forms dark longitudinal stripes in the ablation area (Fig. 1a). Numerous transverse dark bands with exposed mineral dust, mainly upstream of ST2c, were also observed. Both dark and clean surfaces were therefore found around each stake. In 2022, we did not distinguish between dark and clean surfaces during sampling; however, in 2023 and 2024, we sampled both types for BB albedo measurement and impurity collection. BB albedo was measured five times at each site using paired pyranometers (CMP-3, Prede Co., Ltd., wavelength region: $\lambda = 300\text{--}2800$ nm) oriented both upward and downward, parallel to the glacier surface and level with the sky. The average and standard deviation were calculated to obtain representative annual BB albedo values for each stake.

150

155

160

After measuring the BB albedo, we collected impurity samples using a stainless-steel scoop. Samples for OM and MD measurements, including the entire surface granular ice layer with impurities, were placed in a plastic bag. After collecting the samples, we measured the area of the sampled square



165 (length and width) and the sampling depth (i.e., the thickness of the granular ice) at four points along
the sides of the sampling square. The plastic bag containing the samples was brought to base camp,
where the ice was melted over the course of one day, leaving the deposited impurities. All deposited
impurities were then transferred to 30 ml plastic bottles containing 1% formalin.

In the laboratory, the samples were dried in pre-weighed crucibles at 60 °C for 1-2 days. The dry
170 weight of impurities (MD and OM) were then measured. To remove OM, dried samples were
combusted at 500°C for 3 hours in an electric furnace. These methods were based on Takeuchi and Li
(2008), as modified from Dean (1974). Finally, MD and OM amounts per area were calculated using
the sampling area.

The amount of OM was calculated by burning the sample in an oven at 500°C and measuring the
175 weight difference before and after burning. BC is difficult to burn at 500°C (Leifeld, 2007), so it is
highly likely that it was measured as part of the mineral mass (i.e., MD contains BC), but the amount
of BC measured using a different sample from the same location is four orders of magnitude smaller
than that of MD (Section 3.2 and 3.3), so the effect can be ignored.

Samples for BC analysis were collected only in 2024. BC measurement results were detailed in
180 Ueda et al. (2025a). After measuring the BB albedo, we also collected surface granular ice samples
for BC analysis. We collected 41 BC samples in 2024. We used a stainless steel shovel to scoop all
layers of granular ice from a square area about 10 cm on each side and placed them in an additive-free
low-density polyethene bag. This material generates almost no particles. Once melted, each sample
was thoroughly stirred and immediately transferred to 30 ml or 50 ml glass bottles (SV30 and SV50;
185 Nichiden Rika Glass Co., Ltd.). During transport and storage, samples were kept refrigerated and
unfrozen to prevent BC loss from refreezing. Details of the measurement system used in this study
and the evaluation results of the sample storage method for BC measurements were reported by Ueda
et al. (2025b). In the laboratory, we attempted to measure BC concentration using a system consisting
of a pneumatic nebulizer (Marin-5; Cetac Technologies Inc., USA) and a single-particle soot
190 photometer (SP2: Droplet Measurement Technologies (DMT), Longmont, CO, USA) (Mori et al.,
2016; Sinha et al., 2018). A standard SP2 measures the mass of each BC particle with mass equivalent
diameter (DBC) within the 70–850 nm range by assuming a BC particle density of 1.8 g cm⁻³ (Moteki
et al., 2010), whereas the SP2 used for this study measures masses of BC particles within the 70–3000
nm range by expanding the upper limit of the detected incandescence signal in the standard SP2 (Mori
195 et al., 2016). BC mass concentration was obtained by integrating the mass of BC particles. The
impurity sample in surface granular ice contains a significant amount of non-BC material, including
MD and OM. Before measurement using the nebulizer-SP2 system, liquid samples in glass vials were
sonicated for 10 min to minimize the loss of BC particles attached to the other LAI and the vial wall.
To prevent clogging of the nebulizer-SP2 system, after settling of large dust particles by standing for
200 10 min after sonication for all samples, suspended liquid samples in vial middles were dispensed into



205

10 ml PET vials (JST-R/N10; Nikko Hansen & Co., Ltd.), and then measured using the nebulizer-SP2 system. At dispensing, samples were diluted 3–10 times with Milli-Q water based on turbidity. The nebulizer-SP2 system measures the mass of BC per volume of water. During MD measurements at the same site, we measured ice density and sampling area, which were used to calculate BC per area.

2.2.3 Ablation rate of the glacier and ice temperature profile at the surface layer

210 Glacier surface decline was observed using stakes at approximately 5-day intervals during the melt season from 2022 to 2024. Details of the stake measurements are provided in Khalzan et al. (2022), and stake locations are shown in Fig. 1b of Khalzan et al. (2022). The surface decline was converted to mass balance, assuming an ice surface density of 900 kg m^{-3} . Because snow accumulation on the glacier was limited, negative mass balance was considered equivalent to ablation. Daily mean values were calculated for each observation interval. These values were then used to determine the mean velocity over the sampling period. At sites ST1c–ST4c, three stakes (centre, R, and L) were installed
215 at the same elevation in the transverse direction. At ST5c, two stakes (R and L) were installed. To estimate representative daily ablation at each elevation, the mean of the stakes at that elevation was used.

Ice temperatures up to 1 m or 2 m in depth were measured at ST2c and ST5r in 2023. The sensor was set at depths of 1, 0.5, or 0.2 m or at 2 or 1 m. The measurement interval was 15 minutes.
220 Measurements were conducted using a HOBO data logger (model: MX1105). This logger was equipped with an SD-TEMP sensor with an accuracy of $\pm 0.15 \text{ }^\circ\text{C}$. Changes in sensor depth associated with surface melting are discussed in Section 3.1.

2.2.4 Spectral albedo of the weathering crust

225

Spectral albedo of the glacier surface was measured with a spectrometer system on 24 July 2024. The spectrometer system consists of two spectrometer devices for different spectral domains of $\lambda = 350\text{--}1100 \text{ nm}$ (Ocean-HDX, Ocean Insight, Inc.) and $\lambda = 900\text{--}1600 \text{ nm}$ (NIRQuest+1.7, Ocean Insight, Inc.). The spectral albedo is the spectral fraction of the reflected component of the surface to the downward radiant flux density. To measure these flux densities accurately, we used a device using a white reflectance standard (WRS, Spectralon, Labsphere Inc.) and a rotating mount for directing the optical fiber from the spectrometers to WRS, following the setup described in Aoki et al. (2000). The WRS was positioned parallel to the glacier surface. To ensure measurement accuracy, calibration was performed to correct for a fraction of the field of view seen from the WRS obstructed by an optical
230 fiber arm and to verify the cosine property (the ability of the WRS to reflect light isotropically, following the cosine law) of the WRS, as in Aoki et al. (2000).
235



All measurements were conducted in a unified sequence. Five repeated measurements, alternating between upward and downward, were taken, and the five albedos were averaged for each surface condition. We identified two surface types in the area around ST2c: dark and clean surfaces. Spectral albedo was measured for both the weathering crust surface and after granular ice removal (which covered approximately 2 m²). The WRS height above the glacier surface was measured at 40 cm. After spectral albedo measurements, we performed impurity sampling with quadrats, including the granular ice layer. Granular ice thickness was measured at four quadrangle sides. For all samples, granular ice was loosened, placed on black felt, photographed, and the diameter of ice grains was measured with ImageJ (<https://imagej.net/ij/>). LAIs (light-absorbing impurities: MD, OM, and BC) were analysed by the same method as in the previous section. Spectral albedo measurements were also performed for the bubble-rich ice underlying the granular ice layer, but impurity sampling was not carried out for this layer.

2.2.5 Analysis of humic substances

Humic substances, complex mixtures of partially decomposed OM, were extracted from the LAI samples using the NAGOYA method (Kuwatsuka et al., 1992; Ikeya and Watanabe, 2003). Briefly, humic and fulvic acids were extracted with 0.1 M NaOH at a rate of 300 ml g⁻¹ soil carbon (5 ml g⁻¹ for 2023 samples due to low carbon content) by shaking for 24 h at 25 °C under a N₂ atmosphere. The extract was acidified to pH 1.5 with 3 M H₂SO₄, allowed to stand overnight, and centrifuged to separate humic acids (precipitate) from the supernatant, which included fulvic acids (fulvic fraction). The fulvic fraction was applied to the column packed with Supelite DAX-8 (Supelco, Bellefonte, PA, USA) to which fulvic acids are adsorbed, and the amount of fulvic acids on a carbon basis was obtained by subtracting the amount of carbon in the eluate from that in the fulvic fraction applied to the column. For blank correction, 0.05 M H₂SO₄ was used instead of the sample solution. Organic carbon concentration in the solution sample was measured using a total organic carbon analyzer (TOC-VCPH, Shimadzu) after purging with N₂ to remove CO₂. The precipitated humic acids were re-dissolved in 0.1 M NaOH, and the absorbance at 600 nm (A_{600}) and 400 nm (A_{400}) was immediately measured using a spectrophotometer (UV-2450, Shimadzu). A portion of each fraction was diluted 5-fold with 0.067 M KH₂PO₄, and the organic carbon concentration was determined. The degree of humification of humic acids was evaluated using two variables: A_{600}/C and $\log(A_{400}/A_{600})$, where C is the organic carbon concentration (mg mL⁻¹). Humic acids were classified into four types: A, B, P, and Rp according to $\log(A_{400}/A_{600})-A_{600}/C$ diagram (Ikeya and Watanabe, 2003).

270

2.2.6 X-ray diffraction analysis of impurities



275 X-ray diffraction analysis (XRD) was conducted to investigate the mineralogical composition of the
impurity samples on the glacier surface. Samples were collected from each stake with a steel scoop
and placed in polyethene bottles. The samples were then dried at 60°C, powdered, and analyzed by
XRD using a Rigaku Ultima IV diffractometer at Chiba University, Japan. The X-ray target was CuK
 α (copper K alpha radiation), tube voltage 40 kV, and tube current 25 mA. Scans were performed from
4° to 60° (2 θ), where 2 θ represents the angle between the incident and diffracted X-rays, at a rate of 2°
min⁻¹ (2 θ) (Nagatsuka et al., 2014).

280

3 Results and Discussion

3.1 Profile of ice temperature and ice density at the shallow layer

285

Surface melting causes surface lowering, which changes the depths of ice temperature sensors.
Based on surface-lowering rate data collected about every 5 days, we assumed a constant rate
between measurements. Using this, we calculated the daily positions of ice temperature sensors. For
scatter plots of depth versus temperature (Fig. 2), we used the ice temperature readings at local noon.
290 Figure 2 shows temperate ice reaching 0.35 m at ST2c and 0.60 m at ST5r by mid-summer 2023.
The temperate layer at ST5r is thicker than at the lower-elevation ST2c, likely because ST2c has
thinner winter snow cover. As a result, information on low winter temperatures was stored at ST2c,
while thicker snow at ST5r provides more insulation, reducing glacier cooling at ST5r compared to
ST2c.

295 Weathering crust forms when solar radiation penetrates the ice and is absorbed, causing internal
melting at 0°C (Christner et al., 2018; Woods et al., 2023). Then, the weathering crust can be
considered equivalent to temperate ice.

300 These results differ from previous studies, which found that the weathering crust (the upper
porous layer of melting ice) develops to depths greater than 1 m in Greenland (Cooper et al., 2018)
and 2 m in Alaska (Christner et al., 2018). In contrast, on the Potanin Glacier, the weathering crust
was much thinner, with a maximum thickness of only 0.6 m.

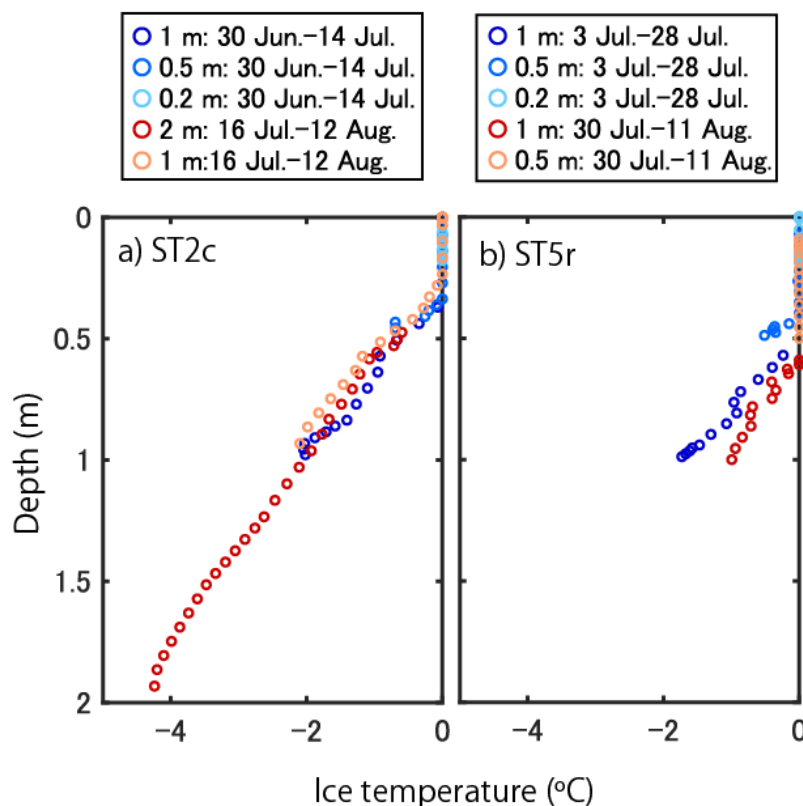


Figure 2. Daily ice temperature profiles at ST2c (a) and ST5r (b) in 2023. Sensor depths were
305 corrected using surface decline data obtained from stake observations. Each legend shows the first
setting depths of the ice temperature sensor, and the measurement date.

Density profiles of ice were obtained for ST2c and ST3c (Fig. 3). The surface layer is 20 mm
thick for ST2c and 100 mm for ST3c, with a density of 300–500 kg m⁻³. Below this low-density
310 surface, the density rises to 700–850 kg m⁻³, close to the typical solid ice density of about 917 kg m⁻³.
The profile shows abrupt changes with depth; ice density increases above 700 kg m⁻³, and the
boundary is clearly identified using a scoop. The surface granular ice layer consists of either
individual particles or fragile, porous granular ice, i.e., loosely packed grains with many air gaps
(Fig. S1a, b). In contrast, the underlying weathering crust contains many air bubbles and is mostly
315 closed off (Fig. S1c). In this study, we refer to this type of ice as “bubble-rich ice,” as shown in Figs.
3 and 4.

Furthermore, ice core observations indicate that within approximately 30–50 cm below the



320 surface, the ice appears white and turbid due to air bubbles, representing a weathering crust - that is,
a 0 °C layer where melting occurs. The surface layer is characterized by strong transmission and
absorption of solar radiation, as well as a high concentration of impurities. As a result, melting
between ice grains is enhanced, leading to the formation of granular ice. In contrast, the underlying
bubble-rich ice exhibits lower transmission and absorption of solar radiation than the surface layer,
and because the air bubbles are not interconnected, impurities cannot penetrate into this layer.
325 Consequently, it has not yet transformed into granular ice. However, with further absorption of solar
radiation, the bubbles may begin to interconnect, allowing impurities to infiltrate, which would in
turn enhance solar absorption.

Because weathering crust development increases albedo (Tedstone et al., 2020), this study uses the
thickness of the low-density granular ice layer (a loosely packed, porous surface ice formed from
melting and refreezing) at the top of the weathering crust as a physical parameter to compare albedo
330 and weathering crust development.

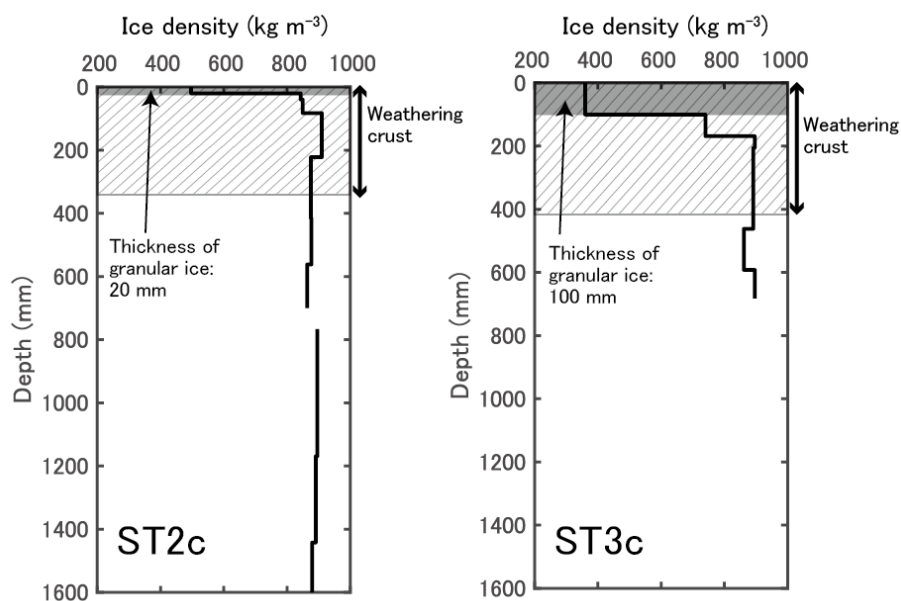
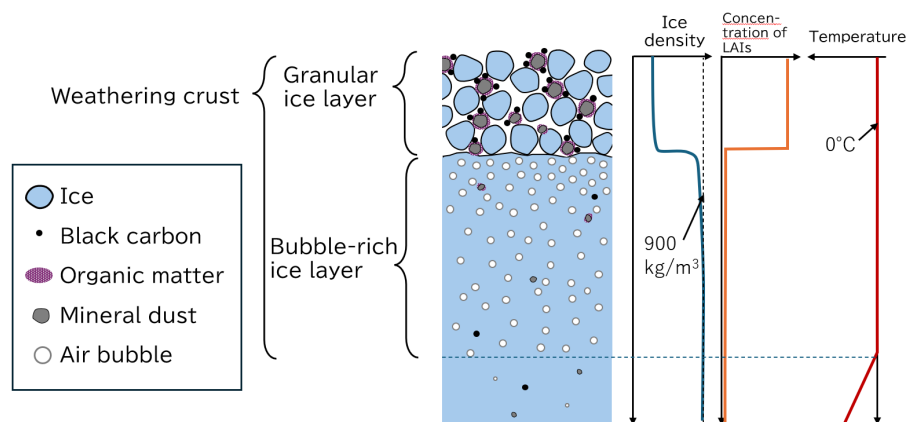


Figure 3. Ice density profile at ST2c (left) and at ST3c (right) at the surface layer. The grey areas indicate layers of weathering granular ice. The weathering crust thickness estimated from ice
335 temperature is indicated by the hatched area.



340 **Figure 4.** Conceptual diagram of weathering crust structure: granular ice layer and bubble-rich ice layer underlying granular ice layer. High content of mineral dust covered with OM and BC in the granular ice layer. And high content of air bubbles and less impurities in the bubble-rich ice layer. Conceptual depth profiles of ice density, LAI content, and ice temperature based on observed data.

345 3.2 Altitudinal distribution of BB albedo, granular ice thickness and impurities

Figure 5 shows the mean and standard deviation of MD, OM, BC, and GIT ABL for each stake and year from 2022 to 2024. Sampling at ST1c was not conducted in 2023 or 2024. Analysis of OM from the clean area at ST4c in 2023 was not conducted. The Potanin Glacier surface clearly contrasts impurity-rich and impurity-poor areas; This contrast is likely governed by the distribution of medial moraines and by mineral exposure resulting from ice melt. In clean areas with fewer impurities, higher BB albedo reduces melting and creates elevated features. Thus, dark and clean surfaces are easily distinguished in the field.

350 The averages of BB albedo, GIT, MD, and OM% (organic matter ratio) from 2022 to 2024 were 0.33 (range: 0.15–0.64), 28.6 mm (range: 3.9–95.0 mm), 75.7 g m⁻² (range: 4.0–248.5 g m⁻²), and 6.5% (range: 1.0–15.0%), respectively. The BC concentration measured in 2024 was 86 ng g⁻¹ (range: 31–289 ng g⁻¹).

To ensure consistency with previous studies, only data obtained from ice surface samples were compared. The MD values were of the same order of magnitude as those reported for the Urumqi Glacier (200–500 g m⁻²)(8–12%:OM%)(Takeuchi et al., 2008) and the Qiyi Glacier in the Qilian Mountains (30.4–873 g m⁻²)(7–11%:OM%)(Takeuchi et al., 2005), whereas slightly lower values were observed in the Suntar-Khayata Mountain Range, Russian Siberia (0.1–43 g m⁻²)(Takeuchi et al., 2015).



Regarding BC, measurements conducted on the Tibetan Plateau using the thermal–optical method reported concentrations exceeding 3000 ng g⁻¹ in granular ice (Li et al., 2017). Another study found a
365 lower concentration of 369 ng g⁻¹, likely influenced by outflow through meltwater (Zhang et al., 2020).

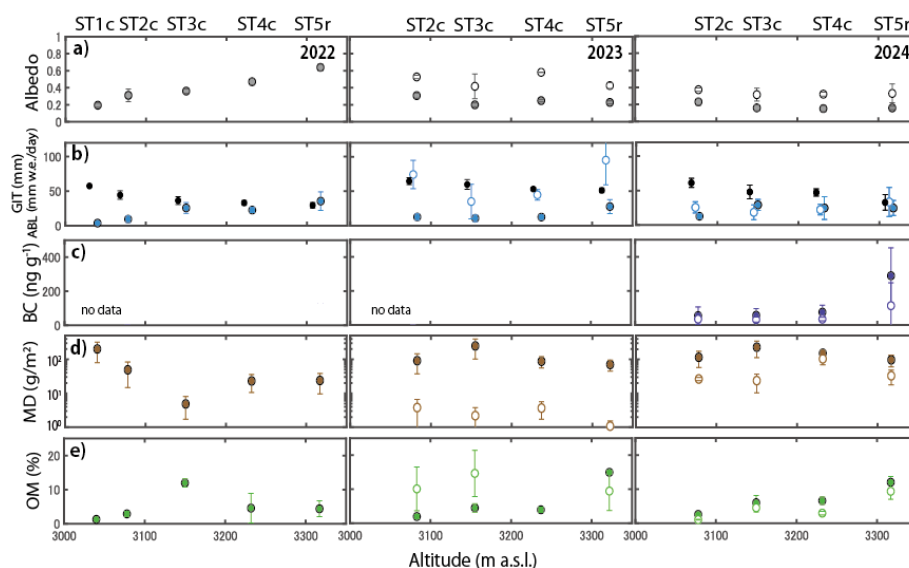
From the graphs of GIT and ABL presented in Fig. 5, it is evident that, when compared with the variations in ABL and GIT, the granular ice layers undergo melting within less than a day. This finding implies that the development and persistence of granular ice layers are highly transient and reflect the prevailing meteorological conditions on the corresponding day.

370 At ST2c, the OM% was consistently lower (2–2.5%) than at the other stakes (4–14%) in all observed samples. This is likely due to numerous outcrops and bands of melt-out MD near ST2, resulting in a high rate of MD exposure. The rate of biological proliferation appears insufficient to keep pace with the rapid exposure of MD, resulting in low OM%. Field observations also indicated that the surface impurities at ST2c were not particularly dark and appeared to reflect the colour of the melt-out MD.

375 In Fig. S2, XRD spectra of MD at each stake are shown. But the diffraction angles of each peak are almost the same at all stakes. The identical XRD peak positions suggest that the MD share a common origin. In the glacier observations, the MD on the glacier surface at ST2c was considered to originate primarily from outcrops melting out of the glacier, whereas at the other stakes, it was thought to derive from rocks that had fallen onto the glacier from the upstream nunatak. However, the results
380 indicated little difference between the mineral compositions in both cases.

In both 2023 and 2024, the dark areas showed similar patterns in granular ice thickness (GIT), mineral dust (MD), and OM% at the sampled sites. In contrast, a pronounced difference was observed between 2023 and 2024 in the clean areas. MD increased substantially in the white areas (from 2–3 g m⁻² in 2023 to 20–30 g m⁻² in 2024), accompanied by a pronounced decrease in OM% (from 9–15% in 2023 to 1–9% in 2024). The thickness of the granular ice also decreased (from more than 35
385 mm in 2023 to less than 33 mm in 2024), and BB albedo values declined (from 0.5 in 2023 to 0.3 in 2024) in the clean area. It is likely that MD deposition occurred between the winter of 2023 and the spring of 2024, resulting in an increase in mineral content per unit area. This, in turn, may have caused a decrease in OM% due to insufficient biological growth keeping pace with the rapid increase in MD.

390 Thus, while the clean areas exhibited substantial changes, the dark areas showed little to no variation. The granular ice thickness was slightly thicker in 2024 than in 2023, and both MD concentrations and OM proportions showed little change between years in the dark area. In the dark areas, MD concentrations were already on the order of 100 g m⁻² in 2023, so even with an additional deposition of approximately 10 g m⁻² in 2024, the order of magnitude remained unchanged. Therefore, it is likely
395 that meteorological conditions in 2024 were generally more favourable for weathering crust (granular ice) development in these portions of the glacier. However, in the clean areas, the granular ice layer was less developed in 2024 compared to 2023. This reason is discussed in Section 3.6.1.



400

Figure 5. Altitudinal distribution of BB albedo a), granular ice thickness (GIT), ablation rate (ABL) b), black carbon (BC) c), mineral dust (MD) d), organic matter ratio (OM%) e). Open circle represents the clean area, while a filled circle indicates the dark area in 2023 and 2024. In panel b), black circles indicate ABL, and blue open circles and blue filled circles denote GIT in the clean and dark areas, respectively. The vertical axis of MD d) is logarithmic. Vertical error bars indicate the standard deviations of each multiple measurement. In 2022, sampling was not conducted separately in dark and clean areas. For 2023 and 2024, filled circles represent data from dark surface areas, whereas open circles represent data from clean surface areas.

405

410 3.3 Spectral albedo of the granular ice and the underlying bubble-rich ice

Spectral albedos of the natural granular ice surface and the underlying bubble-rich ice (Fig. 4) surface were measured in dark and clean surface areas (Fig. 6). Physical properties of granular ice and LAI amount and concentrations in the layer are summarised in Table S1. Although we did not measure

415

LAI beneath the granular ice at the location with observed spectral albedo, it was clear that their concentrations were lower than those in the surface granular ice layer. Ueda et al. (2025a) also reported that shallow ice cores taken at ST3c and ST2c indicated that surface granular ice contains much larger LAI, while underlying ice contains only a few LAI at the Potanin Glacier.

420

During the observation period, the weather conditions were fine, with cloud amount around 2/10. Spectral albedo of dark surface was lower than that of the clean surface in both the visible and near-



infrared spectral regions. In both dark and clean surfaces, the albedo at the granular ice surface was lower than at the ice surface below the granular ice layer at $\lambda > 850$ nm. The reason is the presence of LAIs, mainly in the granular ice layer. At $\lambda > 850$ nm, the spectral albedo of the granular ice surface was higher for both dark and clean ice surfaces than for the underlying ice surface. This would be due to light scattering by the ice particles that compose the surface granular layer in the near-infrared, where LAIs have a weak effect on albedo (Wiscombe and Warren, 1980).

In the visible regions, the bubble-rich ice-surface albedo after removing the darker granular ice layer (blue curve in Fig. 6a) does not increase to the level of the clean granular ice layer (red curve in Fig. 6b). This may be because the albedo of the underlying bubble-rich ice (blue curve in Fig. 6a), measured after removing both surface granular ice and impurities, still contains impurities within the ice crust. It is therefore necessary, in future work, to collect and analyse the impurities contained in the bubble-rich ice layer beneath the granular ice layer.

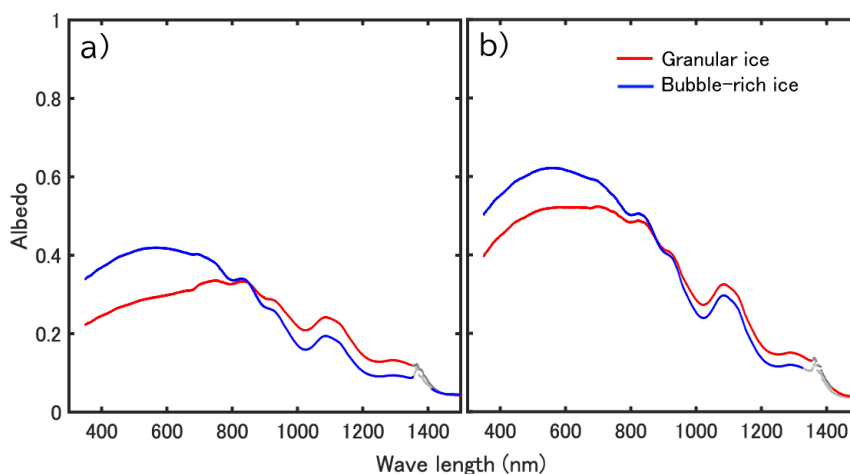


Figure 6. Spectral albedo observed on a) dark and b) clean surfaces at ST2c. Red lines indicate the spectral albedo at the surface of the granular ice. Blue lines indicate bubble-rich ice surface removed from surface granular ice. Physical characteristics of granular ice and the amount of LAIs are summarised in Table S1.

3.4 Humic and fulvic acids

Humic substances contained in surface granular ice were analysed, and the results are summarised in Table 1. The difference in total carbon content between the 2022 and 2023 samples is most likely due to differences in sampling location. Although the 2023 samples contained relatively low amounts of



445 both humic and fulvic acids, the proportions of these fractions in total organic matter on a carbon basis
 were comparable to those typically observed in common soils. (humic acids: 5.9-34%; fulvic acids:
 6.2-24%) (Watanabe and Kuwatsuka, 1991), indicating that the impurities on the Potanin Glacier are
 as humified as the soil. In both years. Both the humic and fulvic acid contents were larger in the finer
 grain size of 53 μm or less, which may reflect the larger surface area of the minerals.

450 Figure S3 shows the diagram indicating the degree of humification of humic acids, which increases
 from the lower left to the upper right. Using this diagram humic acids have been classified into Type
 A, B, Rp, and P. Type A characterized by higher condensed aromatic structures is detected from dark
 soils such as Andisols and Mollisols (Ikeya et al., 2015, 2019), while Type B containing more aliphatic
 structures is observed in brown forest soils such as Inceptisols (Ikeya et al., 2004). Type Rp (meaning
 455 rotten plants), the lowest class with regard to the degree of humification, is frequently detected in
 young soils such as alluvial soils, and Type P, which was initially observed in Podzols and is
 characterized by specific absorptions in UV-visible spectra derived from green pigment (Kumada et
 al., 1967; Ikeya et al., 2019). Humic acids in the impurities of Potanin Glacier are classified as Type P.
 Since A_{600}/C ranged from 1.4 to 2.1, their degree of humification was evaluated as low, corresponding
 460 to Type Rp. Low $\Delta\log(A_{400}/A_{600})$ could be attributed to a pigment, although it was not a green one
 typical of Type P humic acids (data not shown).

Table 1. Results of analysis of humic substances in impurities at the glacier surface.

Sampling year	Particle size μm	Total carbon content mg g^{-1}	Humic acid content $\%^\dagger$	Fulvic acid content $\%^\dagger$	Degree of humification of humic acids	
					$\Delta\log(A_{400}/A_{600})$	A_{600}/C
2022	< 53	26.7	16.2	7.7	0.647	1.57
2022	53 -150	25.8	7.7	6.5	0.588	1.86
2023	< 53	9.2	3.9	4.1	0.630	1.40
2023	53 -150	13.4	2.3	3.3	0.612	2.09

465 † Carbon basis.

3.5 Relation between LAI contents and Granular ice thickness to BB albedo

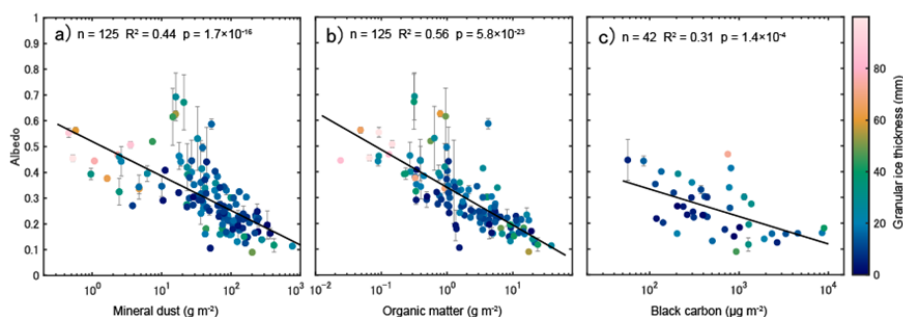
470 For each sample, BB albedo was measured five times, and the relationship between the BB albedo and
 the impurity content per unit area is shown in Fig. 7. The relation between BB albedo and each LAI



(MD, OM and BC) indicates inverse correlation as in previous studies (Takeuchi et al., 2005; Yue et al., 2020). While, observed data showed that the greater the granular ice thickness (GIT), the higher the BB albedo based on observed data (Fig. 8). With increasing thickness of the granular ice layer, the scattering intensity of ice particles enhances, resulting in a further increase in albedo due to the dispersion of light-absorbing impurities (LAIs) into the interstitial spaces or within the granular ice matrix on the surface of the weathering crust. We conclude that the effect of surface granular ice must be taken into account in the ice surface albedo, since the albedo of even these impurity-rich mid-latitude glaciers changes significantly with the development of weathering crust. In other words, on ice albedo, it is necessary to consider not only albedo reduction due to LAIs, but also albedo increase due to granular ice layer development.

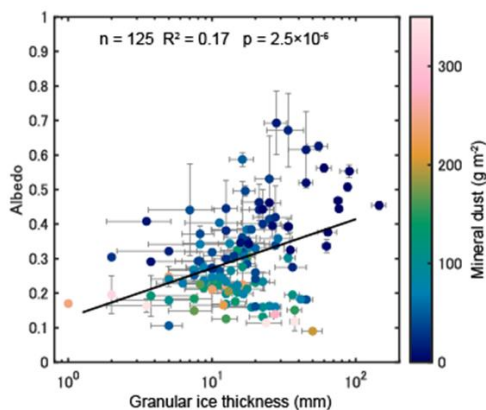
Some samples had low albedo (~ 0.1) even with thicker granular ice layer (2-5 mm), which indicates larger MD are included in granular ice layer in Fig. 8. The year-by-year relationships between LAIs, GIT, and BB albedo for 2022, 2023, and 2024 (Fig. S4) indicate that unlike in 2023 and 2024, the albedo in 2022 was primarily determined by the granular ice thickness, whereas in 2023 and 2024 it was mainly controlled by OM. Table 1 summarises the correlation coefficient between BB albedo and each LAI and WC thickness. All LAIs and GIT are logarithmic. Factors highly correlated with albedo varied widely from year to year, with WC thickness in 2022 and OM in 2023 and 2024. Overall, OM was the most highly correlated with BB albedo. The results indicate that in this glacier, OM predominantly determines albedo and further suggest that it contributes significantly to albedo reduction.

In previous research in Russian Siberia by Takeuchi et al. (2015), total impurities on glaciers were not statistically significantly correlated with surface reflectivity ($\lambda = 0.350\text{-}1.050 \mu\text{m}$), whereas algal biomass showed a significant negative correlation with surface reflectivity.



495

Figure 7. Relation between BB albedo and impurities (MD, OM, BC) a-c). The colour of the circle indicates surface granular ice thickness. All horizontal axes are logarithmic.



500 **Figure 8.** Relation between BB albedo and granular ice thickness (GIT). The circle colour indicates the amount of mineral dust per area.

Table 2. Correlation coefficients (r) between BB albedo and each impurity content or granular ice thickness. (GIT: granular ice thickness, OM: Organic matter, MD: Mineral dust, BC: Black carbon)

505 The amounts of each impurity and GIT are logarithmic. n , r , and p indicate the number of samples, the correlation coefficient, and the p -value, respectively.

year	n		log(GIT) (mm)	log(OM) (g m ⁻²)	log(MD) (g m ⁻²)	log(BC) (μg m ⁻²)
2022	39	r	0.68	-0.43	-0.41	-
		p	1.7×10^{-6}	5.8×10^{-3}	9.8×10^{-3}	-
2023	44	r	0.68	-0.91	-0.85	-
		p	3.4×10^{-7}	3.3×10^{-17}	3.5×10^{-13}	-
2024	42	r	0.11	-0.86	-0.76	-0.55
		p	0.48	3.6×10^{-13}	3.9×10^{-13}	1.4×10^{-4}
2022-2024	125	r	0.41	-0.75	-0.66	-
		p	2.4×10^{-6}	1.7×10^{-23}	3.7×10^{-17}	-

510

Multiple regression analysis results with BBalbedo as the objective variable and impurity and GIT as the explanatory variables are summarised in Table 2. Here, all explanatory variables are in



logarithmic form. In terms of p-values, all explanatory variables (GIT, MD, OM) are statistically significant in 2022. Only OM remains statistically significant in 2023 and 2024. As for the t-value, which should be negative when the explanatory variables have an inverse correlation with the objective variable, it is positive for MD in 2022 and 2024. The multiple regression analysis for the whole year's data, MD, was not statistically significant. The most closely related explanatory variable to BB albedo was OM, followed by GIT, based on the t-values. The following equation is the result of a multiple regression analysis using the data from 2022 to 2024.

520

$$BBAlbedo = 0.0786 \times \log(GIT [mm]) - 0.135 \times \log(OM[g m^{-2}]) + 0.244. \quad (1)$$

Each GIT and OM has a limit on the available range as follows.

525

$$5 \leq GIT \leq 145 \text{ (mm)}, \quad 0.024 \leq OM \leq 23.92 \text{ (g m}^{-2}\text{)}$$

BBalbedo was obtained using equation (10), and RMSE was 0.08.

Based on the comparison of correlation coefficient values from simple correlation analysis (Table 2), as well as the absolute values of the t-statistics from multiple regression analysis (Table 3), it can be inferred that OM has a greater effect on albedo reduction than MD. Furthermore, the relationship between GIT and albedo, as indicated by both simple and multiple regression analyses, shows that GIT increases albedo.

530

Table 3. Summary of multiple regression analysis when the objective variable is BB albedo and the explanatory variables are GIT, MD, OM and BC. All explanatory variables are logarithmic. R² denotes the coefficient of determination, and n indicates the number of samples.

535

	R ²		log(GIT)	log(MD)	log(OM)	log(BC)
year	(n)		(mm)	(g m ⁻²)	(g m ⁻²)	(μg m ⁻²)
2022	0.57 (39)	p	4.2 × 10 ⁻⁶	4.7 × 10 ⁻²	7.8 × 10 ⁻³	-
		t	5.4	2.1	- 2.8	-
2023	0.85 (44)	p	9.4 × 10 ⁻²	0.39	1.4 × 10 ⁻⁶	-
		t	1.7	-0.9	- 5.6	-



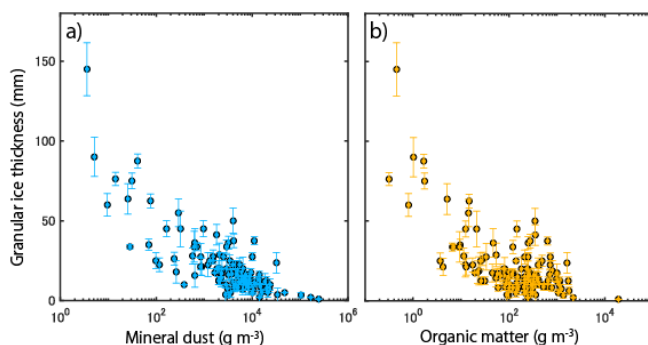
2024	0.75 (42)	p	0.26	0.40	7.8×10^{-3}	0.38
		t	1.1	-0.8	- 2.8	-0.88
2022- 2024	0.60 (125)	p	8.5×10^{-4}	0.64	2.6×10^{-10}	-
		t	3.4	0.5	- 6.9	-

540 3.6 Relation between LAIs and GIT

3.6.1 Relationships of GIT with MD and OM

545 Figure 9 illustrates the relationships between GIT and the concentrations of MD and OM within the granular ice layer. The concentrations were calculated by dividing the amount of impurity per unit area by the granular ice thickness. The results show that higher concentrations of MD and OM lead to thinner GIT, indicating that the granular ice layer cannot grow thick when impurity concentrations are high. The formation of weathering crust and the growth of a thick granular ice layer require the penetration of solar radiation into deeper layers. However, when high concentrations of impurities are present at the surface, incoming solar radiation is absorbed by these impurities in the uppermost layer. As a result, insufficient radiation reaches the deeper ice, thereby inhibiting the thickening of the granular ice layer. Aoki et al. (2011) also demonstrated that higher concentrations of surface impurities reduce the amount of solar radiation transmitted to the underlying layer in a seasonal snowpack. Therefore, when modelling the development of weathering crust (granular ice) in future high-impurity Asian mountain glaciers, the key factor will be the solar radiation absorbed by light-absorbing substances.

555 Regarding the altitude profiles in 2023 and 2024, the MD and GIT values in the dark area were nearly the same, suggesting that the meteorological conditions were comparable (Fig. 5). However, in 2024, the MD concentration in the clean area increased by an order of magnitude, while the weathering crust became thinner. As indicated by the relationship described above, this is likely because an increase in impurities on the glacier surface enhanced surface absorption of solar radiation, decreased transmitted radiation, and consequently led to thinning of the weathering crust.



565 **Figure 9.** Relation between granular ice thickness and mineral dust concentration a) and organic matter
concentration b).

3.6.2 Relationships among the three major light-absorbing impurities

570 Here, we analyse the correlations among the various impurities in Fig. 10. The concentration obtained
by dividing by the GIT is the same as with Fig. 9. We can find a strong correlation between MD and
OM (Fig. 10a), and a statistically significant relationship between OM and BC (Fig. 10b). Fig. 10c
shows no statistical correlation between BC and MD. Several studies in Tibet have reported that BC,
OC, and MD data obtained from snow and ice samples on glaciers are correlated (Zhang et al., 2020;
575 Li et al., 2017), whereas no relationship was observed between BC and MD on the Potanin Glacier.
And also Yala Glacier in the Nepal Himalaya (Takeuchi et al., 2001), Urumqi No.1 Glacier (Takeuchi
and Li, 2008), Qiyi Glacier in Qilian Mountain (Takeuchi et al., 2005)) and glaciers in Suntar-Khayata
Mountain Range, Russian Siberia (Takeuchi et al., 2015) there have also been reports indicating that
OM accounts for 4-12% of the total impurities, and that MD shows a strong correlation with OM.
580 Similarly, a high correlation between OM and MD was observed on the Potanin Glacier in Mongolia.
The OM ratio ranged from 0.5-21.4%, which was much wider than in previous studies.

585

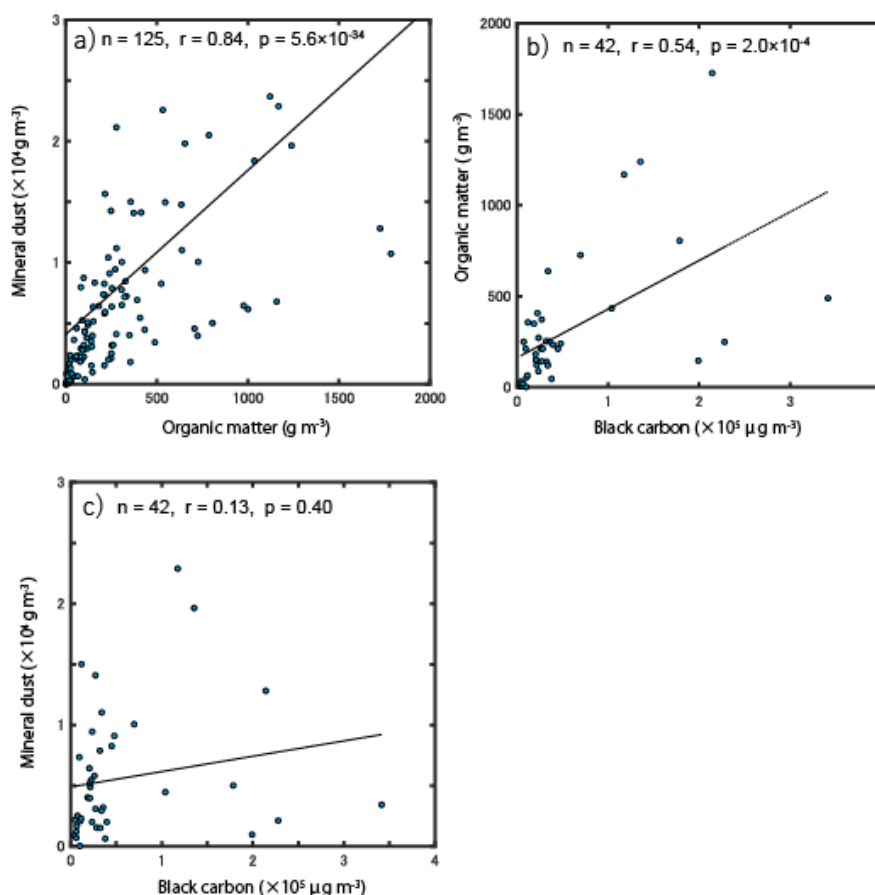


Figure 10. Relationships among the concentrations of the three major light-absorbing impurities on the glacier surface: a) mineral particles and organic matter; b) black carbon and organic matter; c) black carbon and mineral particles. Note that black carbon was sampled only in 2024, so there are only 42 samples.

Analyses of cryoconite granules that settle in small, water-filled circular holes on the ablation zones of glaciers and ice sheets have been extensively conducted. In Greenland, it has been reported that mineral particles serve as condensation nuclei, forming composite particles with organic matter, including extracellular polymeric substances (EPS) and decomposed materials, which are attached to their surfaces (Uetake et al., 2016). Langford et al. (2010) demonstrated that the interstices among mineral particles are filled with organic matter, including pigments and humic substances, and that the mineral particles are surrounded by humified organic matter. The glacier surface in the ablation zone



600 exhibited characteristics similar to those of impurities found within cryoconite holes. Takeuchi et al.
(2015) and Chen et al. (2022) observed cryoconite granules on glacier surfaces composed of minerals
and organic matter containing humic substances. In the glacier surface observed in this study, relatively
large mineral particles were coated with organic matter, which are considered to function as
condensation nuclei. Reports from the Greenland Ice Sheet indicate that MD on the glacier surface
605 plays an important role as a nutrient for snow and ice microorganisms (McCutcheon et al., 2021). In
Asian High Mountains regions, Nagatsuka et al. (2010) analyzed the stable isotopic ratios of strontium
(Sr), neodymium (Nd), and lead (Pb) in surface dust (cryoconite) by separating it into individual
mineral and organic fractions, and demonstrated the potential transfer of nutrients from mineral to
organic phases. Thus, since minerals are also important as nutrient sources for microorganisms,
610 analyses from this perspective will be required in future research.

It was also found that OM shows a significant correlation with BC (Fig. 10b). These findings suggest
that humic substances contain functional groups that likely retain and concentrate BC once it is
deposited on OM. As a result of our analysis, we found that humic substances (humic acid and fulvic
acid) are present in the OM (section 3.5). Humic substances generally possess a variety of functional
615 groups (such as carboxyl and phenolic groups) within their molecular structure, giving them adsorptive
properties (Anesio et al., 2017; Antony et al., 2025). Previous studies have also reported the presence
of cyanobacteria in the ablation zones of other glaciers. Therefore, it is possible that
exopolysaccharides (EPS) secreted by cyanobacteria may be forming biofilms in Potanin Glacier as
well. Thus, the adsorptive properties of humic substances and EPS could contribute to the aggregation
and deposition of BC. However, microbial identification analysis was not performed in this study.
620 These findings indicate that, in addition to albedo reduction caused by microorganisms and humic-
derived organic matter, the adhesive nature of humic substances promotes the enrichment of BC within
glacier surface impurities, thereby providing a structure that can further decrease glacier albedo.

Based on the strength of correlations among LAIs and the properties of each impurity, the
625 relationships among LAIs can be conceptualised as follows: as illustrated in Figure 11, MD produced
by outcrops and weathering serve as the initial substrates. These MDs are thought to serve as
aggregation nuclei for organic matter, with microorganisms and humic substances surrounding their
surfaces. Through the presence of functional groups in humic substances and the formation of biofilms
by EPS, BC becomes concentrated in OM-rich areas. Based on the above scenario, we can
630 hypothesize the process of albedo reduction.

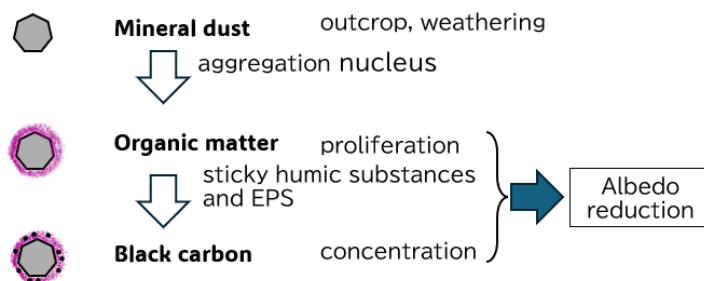


Figure 11. Schematic diagram showing the relationship between the three major LAIs (MD, OM, BC).

635

3.6.3 Limitations and future study

In this study, inverse correlations between broadband albedo and each LAI indicated that LAIs contributed to a reduction in albedo. However, to quantitatively compare the extent to which each LAI contributes to albedo reduction, future work should develop a radiative transfer model representing the observed weathering crust, composed of a granular ice layer containing abundant surface LAIs and an underlying bubble-rich ice layer. For this purpose, it is also necessary to determine the mass absorption coefficient of each LAI.

Regarding BC, the SP2 measures particles in the 70–3000 nm size range, which is considered to capture the majority of the BC mass. Nevertheless, BC particles strongly adhered to coarse mineral grains may have been underestimated due to limitations in the SP2 measurement system's transmission efficiency. Therefore, the sampling procedure needs to be improved so that, in future studies, all BC contained in impurities on the glacier surface can be quantified. As a possible solution, BC in impurity samples can be measured using the thermal–optical method; however, for the Potanin Glacier impurity samples, the concentrations of MD and OM were too high to allow BC quantification by the thermal–optical method.

In this study, the sources of individual impurities were not analyzed. These impurities may originate from atmospheric deposition or exposure of englacial materials, while for organic matter, in situ microbial growth on the glacier surface should also be considered. To better understand the processes governing albedo variations on glaciers, future studies should evaluate the surface mass balance of each impurity, including the portion removed by meltwater flow and examine the relationships between impurity variability, meteorological conditions, and the evolution of the weathering crust layer.

655



660

4 Conclusions

Field observations of shallow ice cores and ice temperature revealed that the weathering crust layer in the ablation zone of Potanin Glacier can be divided into a surface granular ice layer and an underlying bubble-rich ice layer. Our observations of broadband (BB) albedo, granular ice thickness (GIT), and light-absorbing impurity (LAI: mineral dust (MD), organic matter (OM), black carbon (BC)) concentrations indicate that glacier surface albedo is inversely correlated with OM content among the impurities, consistent with prior studies. Additionally, a positive correlation between BB albedo and granular ice thickness was identified. The correlation coefficients between BB albedo and GIT, MD, and OM varied annually, and in some years, no significant correlation was observed between albedo and either GIT or MD. However, across all years, the negative correlation between albedo and OM remained significant. Furthermore, multiple regression analysis of data from 2022–2024 revealed that albedo is strongly related to both GIT and OM, allowing broadband albedo to be robustly estimated by a regression model incorporating these two variables.

675 Analysis of humic substances among the impurities showed that the combined proportion of humic acid and fulvic acid relative to total carbon ranged from 2.3% to 16.2%, demonstrating evidence of soil formation on the glacier surface. Correlation analysis among light-absorbing impurities further suggests MD act as aggregation nuclei for organic matter, with their surfaces supporting microbial adhesion and humic substance accumulation, which in turn facilitate the capture and enrichment of BC on the glacier surface.

680 Measurements of the granular ice thickness indicated that it is typically less than the daily ablation rate, suggesting that the granular ice layer melts completely within a single day and is subsequently renewed from the underlying weathering crust. This process is notably influenced by impurity concentrations: when impurities are abundant, granular ice layers do not thicken appreciably. Going forward, detailed observations of the attenuation coefficient attributable to impurities within granular ice will be crucial for advancing models of granular ice layer evolution on glaciers.

Data availability.

690 Data used in this paper is already saved on Zenodo <https://zenodo.org/uploads/18437674> (now restricted). After the completion of the peer-review process, we will publish.

Author contributions.

Structure of the study: AS, NT, TT, TA, KO. Observation and Sample collection: AS, KP, SM, MO, KK. Sample analysis: AS, KK, MO, SU, SO, AW, KO, NT, SM. Writing (original draft preparation): 695 AS. Funding acquisition: AS, NT, SO, TA. Writing (review and editing): all authors.



Competing Interests

The authors declare that they have no conflict of interest.

700 *Acknowledgements.*

We would like to thank Dr. Noboru Furukawa of Chiba University for helping with XRD analysis. This study is supported by JSPS-KAKENHI (20H00196; 25H00507) and the Transnational Doctoral Program for leading Professional in Asian Countries in Nagoya University.

705

References

- Anesio, A. M., Lutz, S., Chrismas, N. A. M., et al.: The microbiome of glaciers and ice sheets, *npj Biofilms Microbiomes*, 3, 10, <https://doi.org/10.1038/s41522-017-0019-0>, 2017.
- Antony, R., Rossel, P. E., Feord, H. K., Dittmar, T., Tranter, M., Anesio, A. M., and Benning, L. G.: Extraction strategies for profiling the molecular composition of particulate organic matter on glacier surfaces, *Environ. Sci. Technol.*, 59, 4455–4468, <https://doi.org/10.1021/acs.est.4c10088>, 2025.
- 710
- Aoki, T., Fukabori, M., Hachikubo, A., Tachibana, Y., Nishio, F.: Effects of snow physical parameters on spectral albedo and bidirectional reflectance of snow surface, *J. Geophys. Res.*, 105, 10219–10236, <https://doi.org/10.1029/1999JD901122>, 2000.
- 715
- Aoki, T., Hachikubo, A., Hori, M.: Effects of snow physical parameters on shortwave broadband albedos, *J. Geophys. Res.*, 108(D19), 4616, <https://doi.org/10.1029/2003JD003506>, 2003.
- Aoki, T., Kuchiki, K., Niwano, M., Kodama, Y., Hosaka, M., Tanaka, T.: Physically based snow albedo model for calculating broadband albedos and the solar heating profile in snowpack for general circulation models, *J. Geophys. Res.*, 116, D11114, <https://doi.org/10.1029/2010JD015507>, 2011.
- 720
- Braithwaite, R. J.: Positive degree-day factors for ablation on the Greenland ice sheet studied by energy-balance modelling, *J. Glaciol.*, 41, 153–160, <https://doi.org/10.3189/S0022143000017846>, 1995.
- Chen, Y., Takeuchi, N., Wang, F., and Li, Z.: Characteristics of chemical solutes and mineral dust in ice of the ablation area of a glacier in the Tien Shan Mountains, Central Asia, *Front. Earth Sci.*, 10, 904261, <https://doi.org/10.3389/feart.2022.904261>, 2022.
- Christner, B. C., Lavender, H. F., Davis, C. L., Oliver, E. E., Neuhaus, S. U., Myers, K. F., Hagedorn, B., Tulaczyk, S. M., Doran, P. T., Stone, W. C.: Microbial processes in the weathering crust aquifer of a temperate glacier, *The Cryosphere*, 12, 3653–3669, <https://doi.org/10.5194/tc-12-3653-2018>, 2018.
- 730
- Cook, J. M., Hodson, A. J., Irvine-Fynn, T. D. L.: Supraglacial weathering crust dynamics inferred from cryoconite hole hydrology, *Hydrol. Process.*, 30, 433–446,



- <https://doi.org/10.1002/hyp.10602>, 2016.
- 735 Cook, J. M., Hodson, A. J., Taggart, A. J., Mernild, S. H., Tranter, M.: A predictive model for the spectral "bioalbedo" of snow, *J. Geophys. Res.-Earth Surf.*, 122, 434–454, <https://doi.org/10.1002/2016JF003932>, 2017a.
- Cook, J. M., Hodson, A. J., Gardner, A. S., Flanner, M., Tedstone, A. J., Williamson, C., Irvine-Fynn, T. D. L., Nilsson, J., Bryant, R., Tranter, M.: Quantifying bioalbedo: a new physically based model and discussion of empirical methods for characterising biological influence on ice and snow albedo, *The Cryosphere*, 11, 2611–2632, <https://doi.org/10.5194/tc-11-2611-2017>, 2017b.
- 740 Cooper, M. G., Smith, L. C., Rennermalm, A. K., Miège, C., Pitcher, L. H., Ryan, J. C., Yang, K., Cooley, S. W.: Meltwater storage in low-density near-surface bare ice in the Greenland ice sheet ablation zone, *The Cryosphere*, 12, 955–970, <https://doi.org/10.5194/tc-12-955-2018>, 2018.
- Dean, W. E.: Determination of carbonate and organic matter in calcareous sediments and sedimentary rocks by loss on ignition; comparison with other methods, *J. Sediment. Res.*, 44, 242–248, 1974.
- 745 Di Mauro, B., Fugazza, D.: Pan-Alpine glacier phenology reveals lowering albedo and increase in ablation season length, *Remote Sens. Environ.*, 279, 113119, <https://doi.org/10.1016/j.rse.2022.113119>, 2022.
- Flanner, M. G., Zender, C. S.: Linking snowpack microphysics and albedo evolution, *J. Geophys. Res.*, 111, D12208, <https://doi.org/10.1029/2005JD006834>, 2006.
- 750 Flanner, M. G., Zender, C. S., Randerson, J. T., Rasch, P. J.: Present-day climate forcing and response from black carbon in snow, *J. Geophys. Res.*, 112, D11202, <https://doi.org/10.1029/2006JD008003>, 2007.
- Flanner, M. G., Arnheim, J. B., Cook, J. M., Dang, C., He, C., Huang, X., Singh, D., Skiles, S. M., Whicker, C. A., Zender, C. S.: SNICAR-Adv3: a community tool for modeling spectral snow albedo, *Geosci. Model Dev.*, 14, 7673–7704, <https://doi.org/10.5194/gmd-14-7673-2021>, 2021.
- 755 Greuell, W., Smeets, P.: Variations with elevation in the surface energy balance on the Pasterze (Austria), *J. Geophys. Res.*, 106, 31717–31727, 2001.
- Halbach, L., Chevrollier, L. A., Doting, E. L., Fahrner, S., Langford, H., McCutcheon, J., Pearce, D. A., Rassner, S. M. E., and Edwards, A.: Pigment signatures of algal communities and their implications for glacier surface darkening, *Sci. Rep.*, 12, 17643, 2022.
- 760 Hartl, L., Felbauer, L., Schwaizer, G., Fischer, A.: Small-scale spatial variability in bare-ice reflectance at Jamtalferner, Austria, *The Cryosphere*, 14, 4063–4081, <https://doi.org/10.5194/tc-14-4063-2020>, 2020.
- Hugonnet, R., McNabb, R., Berthier, E., Menounos, B., Nuth, C., Girod, L., Farinotti, D., Huss, M., Dussaillant, I., Brun, F., Kääb, A.: Accelerated global glacier mass loss in the early twenty-first century, *Nature*, 592, 726–731, <https://doi.org/10.1038/s41586-021-03436-z>, 2021.
- 765 Ikeya, K., Watanabe, A.: Direct expression of an index for the degree of humification of humic acids using organic carbon concentration, *Soil Sci. Plant Nutr.*, 49, 47–53,



- <https://doi.org/10.1080/00380768.2003.10409978>, 2003.
- 770 Ikeya, K., Maie, N., Han, X., Wang, G., Watanabe, A.: Comparison of carbon skeletal structures in black humic acids from different soil origins, *Soil Sci. Plant Nutr.*, 65, 109–113, <https://doi.org/10.1080/00380768.2019.1584016>, 2019.
- Irvine-Fynn, T. D., Cook, J. M., Edwards, A., Mowlem, M. C., Hodson, A. J., Tranter, M.: Storage and export of microbial biomass across the western Greenland ice sheet, *Nat. Commun.*, 12, 3960, <https://doi.org/10.1038/s41467-021-24109-3>, 2021.
- 775 Khalzan, P., Sakai, A., Fujita, K.: Mass balance of four Mongolian glaciers: In-situ measurements, long-term reconstruction and sensitivity analysis, *Front. Earth Sci.*, 9, 785306, <https://doi.org/10.3389/feart.2021.785306>, 2022.
- Khalzan, P., Sadyrov, S., Sakai, A., Tanak, K., Fujita, K.: Glacier meltwater contribution to river runoff in Western Mongolia, *J. Hydrol.: Regional Studies*, 59, 102375, 780 <https://doi.org/10.1016/j.ejrh.2025.102375>, 2025.
- Kumada, K., Watanabe, A., Uchida, Y., Saigusa, M.: Studies on the humus composition of Japanese soils, *Soil Sci. Plant Nutr.*, 13, 1–8, 1967.
- Kuwatsuka, S., Watanabe, A., Itoh, K., Arai, S.: Comparison of two methods of preparation of humic and fulvic acids, IHSS method and NAGOYA method, *Soil Sci. Plant Nutr.*, 38, 23–30, 785 <https://doi.org/10.1080/00380768.1992.10416948>, 1992.
- Leifeld, J.: Thermal stability of black carbon characterised by oxidative differential scanning calorimetry, *Org. Geochem.*, 38, 112–127, <https://doi.org/10.1016/j.orggeochem.2006.08.004>, 2007.
- Li, X., Kang, S., He, X., Qu, B., Tripathee, L., Jing, Z., Paudyal, R., Li, Y., Zhang, Y., Yan, F., Li, G., 790 Li, C.: Light-absorbing impurities accelerate glacier melt in the central Tibetan Plateau, *Sci. Total Environ.*, 587–588, 310–319, 2017.
- McCutcheon, J., Lutz, S., Williamson, C., Cook, J. M., Tedstone, A. J., Vanderstraeten, A., Wilson, S. A., Stockdale, A., Bonneville, S., McQuaid, J. B., Tranter, M., Hawkings, J., Wadham, J., and Irvine-Fynn, T.: Mineral phosphorus drives glacier algal blooms on the Greenland Ice Sheet, *Nat. Commun.*, 12, 570, <https://doi.org/10.1038/s41467-020-20627-w>, 2021. 795
- Mori, T., Moteki, N., Ohata, S., Koike, M., Goto-Azuma, K., Miyazaki, Y., Kondo, Y.: Improved technique for measuring the size distribution of black carbon particles in liquid water, *Aerosol Sci. Technol.*, 50, 242–254, <https://doi.org/10.1080/02786826.2016.1147644>, 2016.
- Moteki, N., Kondo, Y., Nakamura, S.: Method to measure refractive indices of small nonspherical 800 particles: application to black carbon particles, *J. Aerosol Sci.*, 41, 513–521, <https://doi.org/10.1016/j.jaerosci.2010.02.013>, 2010.
- Nagatsuka, N., Takeuchi, N., Nakano, T., Kokado, E., and Li, Z.: Sr, Nd and Pb stable isotopes of surface dust on Ürümqi glacier No. 1 in western China, *Ann. Glaciol.*, 51, 95–



- 105, <https://doi.org/10.3189/172756411795931895>, 2010. Nagatsuka, N., Takeuchi, N., Uetake,
805 J., Shimada, R.: Mineralogical composition of cryoconite on glaciers in northwest Greenland,
Bull. Glaciol. Res., 32, 107–114, <https://doi.org/10.5331/bgr.32.107>, 2014.
- Naegeli, K., Huss, M.: Sensitivity of mountain glacier mass balance to changes in bare-ice albedo,
Ann. Glaciol., 58, 119–129, <https://doi.org/10.1017/aog.2017.25>, 2017.
- Onuma, Y., Takeuchi, N., Tanaka, S., Nagatsuka, N., Niwano, M., Aoki, T.: Physically based model of
810 the contribution of red snow algal cells to temporal changes in albedo in northwest Greenland,
The Cryosphere, 14, 2087–2101, <https://doi.org/10.5194/tc-14-2087-2020>, 2020.
- Painter, T. H., Duval, B., Thomas, W. H.: Detection and quantification of snow algae with an airborne
imaging spectrometer, *Appl. Environ. Microbiol.*, 67, 5267–5272,
<https://doi.org/10.1128/AEM.67.11.5267-5272.2001>, 2001.
- 815 Pan, C. G., Kamp, U., Munkhjargal, M., Halvorson, S. J., Dashtseren, A., Walther, M.: An estimated
contribution of glacier runoff to Mongolia's Upper Khovd River Basin in the Altai Mountains,
Mt. Res. Dev., 39, 12–20, <https://doi.org/10.1659/MRD-JOURNAL-D-18-00059.1>, 2019.
- Pan, C. G., Pope, A., Kamp, U., Dashtseren, A., Walther, M., Syromyatina, M. V.: Glacier recession in
the Altai Mountains of Mongolia in 1990–2016, *Geogr. Ann. A Phys. Geogr.*, 100, 1–19,
820 <https://doi.org/10.1080/04353676.2017.1407560>, 2017.
- Pellicciotti, F., Brock, B., Strasser, U., Burlando, P., Funk, M., Corripio, J.: An enhanced temperature-
index glacier melt model including the shortwave radiation balance: development and testing for
Haut Glacier d'Arolla, Switzerland, *J. Glaciol.*, 51, 573–587,
<https://doi.org/10.3189/172756505781829124>, 2005.
- 825 Picard, G. and Libois, Q.: Simulation of snow albedo and solar irradiance profile with the Two-streAm
Radiative TransfER in Snow (TARTES) v2.0 model, *Geosci. Model Dev.*, 17, 8927–8953,
<https://doi.org/10.5194/gmd-17-8927-2024>, 2024.
- Sinha, P.R., Kondo, Y., Goto-Azuma, K., Tsukagawa, Y., Fukuda, K., Koike, M., Mori, T., Oshima, N.,
Førland, E.J., Irwin, M., Gallet, J.-C. and Pedersen, C.A.: Seasonal progression of the deposition
830 of black carbon by snowfall at Ny-Ålesund, Spitsbergen, *J. Geophys. Res. Atmos.*, 123, 997–
1016, doi:10.1002/2017JD028027, 2018.
- Skiles, S. M., Painter, T. H.: Daily evolution in dust and black carbon content, snow grain size, and
snow albedo during snowmelt, Rocky Mountains, Colorado, *J. Glaciol.*, 63, 118–132,
<https://doi.org/10.1017/jog.2016.125>, 2017.
- 835 Takeuchi, N., Kohshima, S., Seko, K.: Structure, formation, and darkening process of albedo reducing
material (cryoconite) on a Himalayan glacier: a granular algal mat growing on the glacier, *Arct.
Antarct. Alp. Res.*, 33, 115–122, <https://doi.org/10.2307/1552211>, 2001.
- Takeuchi, N., Matsuda, Y., Sakai, A., Fujita, K.: A large amount of biogenic surface dust (cryoconite)
on a glacier in the Qilian Mountains, China, *Bull. Glaciol. Res.*, 22, 1–8, 2005.



- 840 Takeuchi, N., Li, Z.: Characteristics of surface dust on Ürtimqi Glacier No. 1 in the Tien Shan Mountains, China, *Arct. Antarct. Alp. Res.*, 40, 744–750, [https://doi.org/10.1657/1523-0430\(07-021\), 2008](https://doi.org/10.1657/1523-0430(07-021), 2008).
- Takeuchi, N., Fujisawa, Y., Kadota, T., Tanaka, S., Miyairi, M., Shirakawa, T., Kusaka, R., Fedorov, A. N., Konstantinov, P., Ohata, T.: The effect of impurities on the surface melt of a glacier in the
- 845 Suntar-Khayata mountain range, Russian Siberia, *Front. Earth Sci.*, 3, 82, <https://doi.org/10.3389/feart.2015.00082, 2015>.
- Tedstone, A. J., Cook, J. M., Williamson, C. J., Hofer, S., McCutcheon, J., Irvine-Fynn, T., Gribbin, T., Tranter, M.: Algal growth and weathering crust state drive variability in western Greenland Ice Sheet ice albedo, *The Cryosphere*, 14, 521–538, <https://doi.org/10.5194/tc-14-521-2020, 2020>.
- 850 The GlaMBIE Team: Community estimate of global glacier mass changes from 2000 to 2023, *Nature*, 639, 382–388, <https://doi.org/10.1038/s41586-024-08545-z, 2025>.
- Traversa, G., Di Mauro, B.: Weathering crust formation outpaces melt-albedo feedback on blue ice shelves of East Antarctica, *Commun. Earth Environ.*, 5, 740, <https://doi.org/10.1038/s43247-024-01896-5, 2024>.
- 855 Ueda, S., Sakai, A., Ohata, S., Khalzan, P., Matoba, S., Kondo, K., and Matsui, H.: Concentration and size distribution of black carbon over the ablation area of Potanin glacier: Enrichment ability of surface weathering granular ice of water-insoluble particles with snow/ice melting, *EGUsphere [preprint]*, <https://doi.org/10.5194/egusphere-2025-5301, 2025a>.
- 860 Ueda, S., Ohata, S., Iizuka, Y., Seki, O., Matoba, S., Matsui, H., Koike, M. and Kondo, Y.: Evaluation of sample storage methods for single particle analyses of black carbon in snow and ice: Merits and risks of glass and plastic vials for melted sample storage, *Aerosol Sci. Tech.*, 59, 1–6. doi:10.1080/02786826.2025.2542900, 2025b.
- Uetake, J., et al.: Microbial community variation in cryoconite granules on Qaanaaq Glacier, NW
- 865 Greenland, *FEMS Microbiol. Ecol.*, 92(9), fiw127, <https://doi.org/10.1093/femsec/fiw127, 2016>.
- Watanabe, A., Kuwatsuka, S.: Triangular diagram for humus composition in various types of soils, *Soil Sci. Plant Nutr.*, 49, 167–170, 1991.
- Warren, S. G.: Optical properties of snow, *Rev. Geophys.*, 20(1), 67–89, <https://doi.org/10.1029/RG020i001p00067, 1982>.
- 870 Warren, S. G. and Wiscombe, W. J.: A model for the spectral albedo of snow. II: Snow containing atmospheric aerosols, *J. Atmos. Sci.*, 37, 2734–2745, 1980. Whicker, C. A., Flanner, M. G., Dang, C., Zender, C. S., Cook, J. M., Gardner, A. S.: SNICAR-ADv4: a physically based radiative transfer model to represent the spectral albedo of glacier ice, *The Cryosphere*, 16, 1197–1220, <https://doi.org/10.5194/tc-16-1197-2022, 2022>.
- 875 Wiscombe, W. J. and Warren, S. G.: A model for the spectral albedo of snow. I: Pure snow, *J. Atmos.*



- Sci., 37, 2712–2733, 1980. Woods, T., Hewitt, I. J.: A model of the weathering crust and microbial activity on an ice-sheet surface, *The Cryosphere*, 17, 1967–1987, <https://doi.org/10.5194/tc-17-1967-2023>, 2023.
- 880 Yue, X., Li, Z., Zhao, J., Fan, J., Takeuchi, N., Wang, L.: Variation in albedo and its relationship with surface dust at Urumqi Glacier No. 1 in Tien Shan, China, *Front. Earth Sci.*, 8, 110, <https://doi.org/10.3389/feart.2020.00110>, 2020.
- 885 Zhang, Y., Kang, S., Cong, Z., Schmale, J., Sprenger, M., Li, C., Yang, W., Gao, T., Sillanpää, M., Li, X., Liu, Y., Chen, P., Zhang, X.: Light-absorbing impurities enhance glacier albedo reduction in the southeastern Tibetan plateau, *J. Geophys. Res. Atmos.*, 122, 6915–6933, <https://doi.org/10.1002/2016JD026397>, 2017.
- Zhang Y., Gao T., Kang S., Sprenger M., Tao S., Du W., Yang J., Wang F., Meng W.: Effects of black carbon and mineral dust on glacial melting on the Muz Taw glacier, Central Asia, *Sci. Total Environ.*, 740, 140056, <https://doi.org/10.1016/j.scitotenv.2020.140056>, 2020.